RSC Advances

PAPER

View Article Online
View Journal | View Issue

Cite this: *RSC Adv.*, 2023, **13**, 21459

Beneficial effect of cerium excess on *in situ* grown $Sr_{0.86}Ce_{0.14}FeO_3$–CeO_2 thermocatalysts for the degradation of bisphenol A†

Martin B. Østergaard, *[a] Francesca Deganello, *[b] Valeria La Parola, [b] Leonarda F. Liotta, [b] Vittorio Boffa [a] and Mads K. Jørgensen [a]

Ce-doped $SrFeO_3$ perovskite-type compounds are known as good thermocatalysts for the abatement of wastewater contaminants of emerging concern. In this work, $Sr_{0.86}Ce_{0.14}FeO_3$–CeO_2 perovskite-oxide systems with increasing amounts of cerium excess (0, 5, 10 and 15 mol% Ce), with respect to its maximum solubility in the perovskite, were prepared in one-pot by solution combustion synthesis and the effects of cerium excess on the chemical physical properties and thermocatalytic activity in the bisphenol A degradation were evaluated. The powders were characterized by powder X-ray diffraction combined with Rietveld refinement, X-ray photoelectron spectroscopy, thermal gravimetry, temperature programmed reduction, nitrogen adsorption, scanning electron microscopy and energy dispersive X-ray spectroscopy techniques. Results highlight that the perovskite structural, redox, surface, and morphological properties are affected by the *in situ* co-growth of the main perovskite phase and ceria and that a larger cerium excess has a beneficial effect on the thermocatalytic performance of the perovskite oxide–ceria biphasic system, although ceria is not active as a thermocatalyst itself. Perovskite properties and performance are enhanced by the tetragonal distortion induced by the introduction of cerium excess in the synthesis. It is supposed that a larger oxygen mobility and an easier reducibility are among the most relevant features that contribute to superior thermocatalytic properties of these perovskite oxide-based systems. These results also suggest new perspectives in the nanocomposite preparation and their catalytic applications.

Received 22nd May 2023
Accepted 10th July 2023

DOI: 10.1039/d3ra03404f

rsc.li/rsc-advances

1. Introduction

Perovskite oxides (POs) are mixed metal oxides with the formula ABO_3, where A and B are metal cations coordinated by 12 and 6 oxygen (O) anions, respectively.[1] The A-site is often occupied by di- or tri-valent alkaline earth elements or lanthanides, while the B-site is occupied by transition metals.[2] The properties of POs can be tailored by full or partial substitution of A, B or O sites.[3] Among the interesting properties of POs is the catalytic activity for wastewater pollutant abatement, that greatly depends on their chemical composition, structure, morphology, and texture.[4] The synthesis methodology used to prepare perovskite oxide catalysts can also affect their final properties and needs to be carefully selected.[5] Perovskite oxide powders can be conveniently synthesized by wet chemical synthesis routes.[3] A well-known wet chemical method is the solution combustion synthesis, which provides mixed oxide powders with relatively high surface area and porosity which is beneficial for catalytic use.[6,7]

When POs are associated with metal oxides with different structure and properties, their catalytic properties for wastewater cleaning are often boosted due to the synergetic interaction between the two materials, especially if heterostructures are formed.[8–11] Therefore, PO–oxide biphasic systems have been increasingly investigated as a new strategy to boost catalytic performance of the single PO and oxide components. The PO–oxide systems can be obtained by *in situ* exsolution under particular conditions,[12] by self-assembling one-pot synthesis,[9,10] by impregnation of a metal oxide support[8,13] or mixing the powders after dispersion in a solvent.[11]

Ce-doped $SrFeO_3$ POs have shown great activity in the thermocatalytic abatement of water pollutants and dyes,[14–16] making these materials attractive for environmental applications, such as the final polishing of wastewater effluents and the treatment of produced water.[15–18] Ce-doped $SrFeO_3$ perovskites have been synergistically integrated with membrane filtration units, namely nanofiltration and membrane distillation.[16,19] The advantages of such integration include the degradation of toxic

[a]*Department of Chemistry and Bioscience, Center for Membrane Technology, Aalborg University, Aalborg East, 9220, Denmark. E-mail: mbo@bio.aau.dk*

[b]*Istituto per lo Studio dei Materiali Nanostrutturati, Consiglio Nazionale delle Ricerche, Via Ugo La Malfa 153, 90146, Palermo, Italy. E-mail: francesca.deganello@cnr.it*

† Electronic supplementary information (ESI) available. See DOI: https://doi.org/10.1039/d3ra03404f

pollutants in the membrane concentrate and the mitigation of organic fouling during filtration without any UV or visible light and at temperatures below 80 °C. The un-doped $SrFeO_3$ can be tetragonal, cubic, or orthorhombic, depending on the oxidation state of the iron and on the oxygen content.[20,21] Cubic structure in $SrFeO_3$ is stabilized only when it is fully oxygenated, as it happens after high oxygen pressure treatment, or when is doped with specific cations, as for example cerium, which can replace up to 14 mol% Sr^{2+} at the A-site. For higher doping levels, CeO_2 segregates as secondary phase.[22]

PO–ceria systems based on $SrFeO_3$ or Ce-doped $SrFeO_3$ POs have been already studied in the literature for environment-related catalytic applications. Recently, Tian *et al.* have evaluated the effect of cerium amount in Ce-doped $SrFeO_3$ perovskite systems for the ethane oxidative dehydrogenation coupled with CO_2 splitting, where ceria was exsolved and was recognized to have an important role in the process.[23] Palma *et al.* suggested that segregated ceria phase improves the thermocatalytic activity in degradation of organic pollutants due to an increased number of oxygen vacancies in the perovskite phase.[18] Interestingly, Belessi *et al.* found that the co-presence of $SrFeO_3$ and CeO_2 in a multicomponent lanthanum perovskite-based catalytic system enhanced considerably the catalytic activity in the simultaneous oxidation of NO and CO, due to the mutual redox cycles occurring in the two phases.[24]

Ceria seems to have a mostly positive impact on catalytic reactions as well for other PO–ceria systems,[25–31] with only few exceptions.[32,33] For example, compared to their respective single-phase perovskites, $LaFeO_3$–CeO_2 and $LaCuO_3$–CeO_2 composites have enhanced Fenton-like photocatalytic activity in the degradation of bisphenol F, an emerging wastewater contaminant.[25] The effect of segregated metal oxides has been ascribed to the presence of oxygen vacancies at the surface of the oxides, high oxygen mobility and the crystal orientation.[34] In the case of pure ceria, the catalytic activity was influenced by a cerium–oxygen double bond termination which is a weak bonding improving its catalytic activity when broken, forming oxygen vacancies.[35] Dai *et al.* reported the formation of an interface between $LaFeO_3$ and CeO_2 in $LaFeO_3$–CeO_2 oxide systems, obtained by decoration of $LaFeO_3$ with ceria, with a positive effect on the oxygen evolution reaction ability of the material.[36] The reason of the enhanced performance was a redistribution of cations at the perovskite–ceria interface, resulting in an increased oxygen vacancies concentration and high valence iron.

In this work, the integration of Ce-doped $SrFeO_3$ POs in a biphasic PO-oxide system was studied as a strategy to boost the thermocatalytic activity of Ce-doped $SrFeO_3$ POs, without adding any additional element, that could limit or block the thermocatalytic activity of the perovskite oxide. Cerium was introduced as metal nitrate in a one-pot solution combustion synthesis of a $Sr_{0.86}Ce_{0.14}FeO_3$–CeO_2 system and the CeO_2 was formed upon segregation from the Ce-doped $SrFeO_3$ perovskite oxide by adding to the combustion mixture various molar percentages of cerium over its solubility limit in $SrFeO_3$. The impact of increasing cerium excess (0, 5, 10 and 15 mol% excess) in the PO–ceria system on the properties and thermocatalytic activity of the $Sr_{0.86}Ce_{0.14}FeO_3$–CeO_2 system in the degradation of bisphenol A (BPA) was investigated. Structural properties of bulk and surface perovskite–ceria powders were determined by X-ray diffraction (XRD) and X-ray photoelectron spectroscopy (XPS), respectively. A multistep thermal gravimetric experiment (TGA) was used to estimate the oxygen vacancies. Redox properties were studied by temperature programmed reduction experiments (TPR). Textural properties were investigated by N_2-adsorption with Brunauer–Emmett–Teller (BET) methodology. Morphology was observed by scanning electron microscopy (SEM) and energy dispersive X-ray spectroscopy (EDS).

2. Experimental

2.1. Powders synthesis

Ce-doped $SrFeO_3$ were synthesized by solution combustion synthesis (SCS) with the composition $Sr_{0.86}Ce_{0.14+y}FeO_{3-\delta}$, where y (=0, 0.05, 0.10, and 0.15) denotes excess cerium fraction with respect to the maximum Ce solubility limit of 0.14. Samples are thus named according to their excess cerium amount *Ce0*, *Ce5*, *Ce10*, and *Ce15*. $Sr(NO_3)_2$ (Acros Organics, purity 99+%), $Ce(NO_3)_3 \cdot 6H_2O$ (Sigma Aldrich, purity 99%), and $Fe(NO_3)_3 \cdot 9H_2O$ (Sigma Aldrich, purity ≥98%) were dissolved in 200 mL of distilled water.

After dissolving the metal nitrates, citric acid (Carl Roth, purity ≥99.5%) was added as a fuel to obtain a citric acid-to-metal nitrates ratio of 2, and NH_4NO_3 (Sigma Aldrich, purity ≥99.5%) was added as additional oxidant to get a reducers-to-oxidizers ratio (φ) of 1. Finally, NH_4OH was added to adjust the pH to 6 for all samples. The solution was placed in a 2 L glass beaker in contact with a magnetic stirrer equipped with a heater and a vertex thermocouple to continuously stir the solution while evaporating the water at 80 °C. After evaporation a sticky gel was left in the beaker. The temperature was raised to decompose the gel by self-ignition occurring at temperatures higher than 220 °C. The obtained powder was crushed, followed by calcination at 1000 °C for 5 hours heated at 2 °C min^{-1}.

The calcined powders were suspended in water to remove any residual un-combusted organic material[37,38] followed by filtration. In detail, approx. 2 g of powder (the whole batch) was suspended in 500 mL deionized water, stirred for 1 h at room temperature, and centrifuged at 7000 rpm for 15 min. The supernatant was removed, and the perovskite was rinsed off the tube by water resulting in a new suspension that was filtered using vacuum pump and a 0.45 μm filter. The powder was dried overnight at 105 °C. Additionally, pure CeO_2 was synthesized using the same methodology and conditions. A mechanical mixture (MM) with composition 89.4 wt% *Ce0*–10.6 wt% CeO_2 was prepared by manual grinding with agate pestle and mortar until visible homogenization to investigate differences between a one-pot prepared and mechanically grinded biphasic thermocatalyst. This composition was chosen on purpose to have the same weight percentage of segregated CeO_2 crystalline phase as in *Ce15* according to Rietveld refinements results (see also Section 3.1 on structural characterization results). No thermal treatment was further applied. In Fig. S1,† a picture of

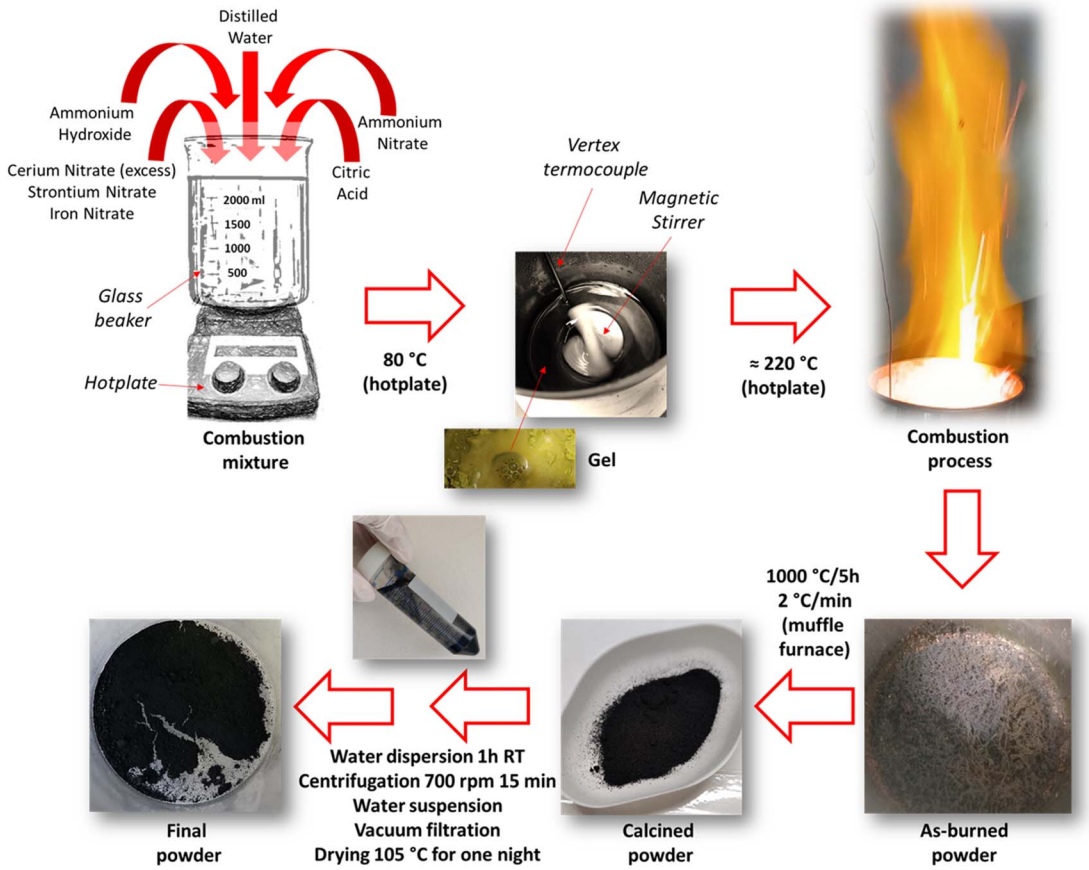

Scheme 1 Schematical description of the solution combustion synthesis procedure used for the preparation of Ce-doped $SrFeO_3$ with cerium excess.

the mechanical mixture before and after grinding is shown. Scheme 1 shows a description of the synthesis procedure used, whereas in Table 1 a legend of the investigated powders is reported.

2.2. Powders characterization

X-ray diffraction (XRD) measurements were carried out on a Bruker-Siemens D5000 X-ray powder diffractometer equipped with a Kristalloflex 760 X-ray generator and with a curved graphite monochromator using Cu Kα radiation (40 kV/30 mA). The 2θ step size was 0.03, the integration time was 20 s per step, and the 2θ scan ranged from 10° to 90°. The powder diffraction patterns were analyzed by Rietveld refinement using the GSAS II software.[39] The compound $Sr_{0.9}Ce_{0.1}FeO_3$ (ICDD PDF4$^+$ inorganic database – PDF card no. 04-014-0169) was chosen as a starting model for the Rietveld Refinement, setting the Sr and the Ce occupancies to 0.86 and 0.14, respectively. A Chebyschev polynomial function with 8 polynomial coefficients was chosen for the background and Pseudo Voigt function was used for the peak profile fitting. In the structure refinement lattice constants, Debye Waller factors, microstrain, and crystallite size were considered as variable parameters. Crystallite size was obtained directly from the GSAS II software output based on the Scherrer equation, microstrain is a unitless number directly

Table 1 Legend of the investigated powders and their nominal composition in mol% and wt%. Nominal wt% of *Ce0*, *Ce5*, *Ce10* and *Ce15* were calculated from the nominal mol% values, whereas nominal Ce mol% of *MM* was deduced from its nominal CeO_2 wt% value

Sample	Nominal composition (mol%)	Nominal composition (wt%)
Ce0	$Sr_{0.86}Ce_{0.14}FeO_3$ + 0 mol% Ce excess	100 wt% $Sr_{0.86}Ce_{0.14}FeO_3$ + 0 wt% CeO_2 excess
Ce5	$Sr_{0.86}Ce_{0.14}FeO_3$ + 5 mol% Ce excess	96.0 wt% $Sr_{0.86}Ce_{0.14}FeO_3$ + 4.0 wt% CeO_2 excess
Ce10	$Sr_{0.86}Ce_{0.14}FeO_3$ + 10 mol% Ce excess	92.0 wt%$Sr_{0.86}Ce_{0.14}FeO_3$ + 8.0 wt% CeO_2 excess
Ce15	$Sr_{0.86}Ce_{0.14}FeO_3$ + 15 mol% Ce excess	88.5 wt% $Sr_{0.86}Ce_{0.14}FeO_3$ + 11.5 wt% CeO_2 excess
CeO_2	CeO_2 (prepared by SCS)	100 wt% CeO_2
MM	$Sr_{0.86}Ce_{0.14}FeO_3$ + 12 mol% Ce excess	89.4 wt% $Sr_{0.86}Ce_{0.14}FeO_3$ + 10.6 wt% CeO_2 excess (mechanical mixture)

from the GSAS II software output and describing a range of lattice constants through the equation $10^{-6}\cdot(\Delta - d)/d$. From fitting results, the structural parameters of the investigated compounds and phase composition and the relative cell edge lengths were obtained. The agreement between fitted and observed intensities and the reliability factors (R_w and χ^2) were acceptable.[40] Standard deviations of the refined cell parameters were automatically estimated by GSAS II software and were always indicated in graphs and tables together with the obtained values. Images of the structures were created using Vesta Software[41] starting from the cif files of the Rieveld outputs.

X-ray photoelectron spectroscopy (XPS) analyses of the powders were performed with a VG Microtech ESCA 3000 Multilab (VG Scientific, Sussex, UK), using Al Kα source (1486.6 eV) run at 14 kV and 15 mA, and CAE analyser mode. For the individual peak energy regions, a pass energy of 20 eV across the hemispheres was used. The constant charging of the samples was removed by referencing all the energies to the C 1s peak energy set at 285.1 eV, arising from adventitious carbon. Analyses of the peaks were performed using the CASA XPS software (version 2.3.17, Casa Software Ltd. Wilmslow, Cheshire, UK, 2009). Gaussian (70%)–Lorentzian (30%), defined in Casa XPS as GL (30) profiles were used for each component of the main peaks after a Shirley type baseline subtraction. The binding energy values are given with an error of ±0.2 eV, whereas the relative percentages of each component are given with an error of ±0.5%.

Thermogravimetric analyses (TGA) were performed with a TGA/DSC1 STAR system Mettler Toledo. The sample (15 mg) was pretreated in N_2 (30 mL min^{-1}) heating from 25 to 500 °C (ramp rate 10 °C min^{-1}) (step 1), holding time at 500 °C for 15 min (step 2), then, it was cooled down under nitrogen atmosphere to 150 °C (step 3). Steps 1 and 2 were performed to remove any adsorbed water, oxygen, or carbonate species. In step 3, the sample was filled with pure O_2 (30 mL min^{-1}) at 150 °C during 1 h (step 4) and cooled to 25 °C still under O_2 (step 5), to fill the oxygen vacancies. Finally, the sample was flowed from room temperature up to 150 °C (30 min) under N_2 (30 mL min^{-1}) to remove physisorbed oxygen species followed by increasing temperature from 150 °C to 800 °C (ramp rate 5 °C min^{-1}) (step 6). During this last step, the removal of any chemisorbed oxygen species occurred and the weight loss between 300–600 °C was considered to evaluate, if present, the surface oxygen vacancies content of the sample. The weight loss above 600 °C corresponds to the amount of bulk oxygen released.

Reduction properties of the oxides were studied by temperature programmed reduction (TPR) measurements in H_2/Ar (5%, 30 mL min^{-1}) in the range between room temperature and 1050 °C (heating rate 10 °C min^{-1}). Experiments were carried out with a Micromeritics Autochem 2910 instrument equipped with a thermal conductivity detector (TCD) for the evaluation of hydrogen consumption with proper calibration curves. The accuracy of hydrogen consumption evaluated through TPR measurements is ±10% and the temperature of peaks is quoted with an uncertainty of ±15 °C. For each sample, about 0.1 g of powder previously calcined at 1000 °C for 5 h was pre-treated in O_2/He (5%, 50 mL min^{-1}) at 300 °C for 1 h and then cooled down under He atmosphere.

Specific surface area (Brunauer Emmett and Teller's method[42]) and pore size distributions (Barrett Joyner and Halenda's method[43]) were evaluated by nitrogen adsorption/desorption measurements at −196 °C, using ASAP 2020 Plus Materials. All the samples were pre-treated under vacuum at 250 °C (10 °C min^{-1} ramp) for 1 h prior to the measurements.

The morphology of samples was imaged using a Zeiss EVO 60 scanning electron microscope (SEM). The SEM was combined with energy dispersive X-ray spectroscopy that was used to record the elemental mapping.

2.3. Catalytic degradation experiments

The catalytic activity of the synthesized perovskites, after calcination at 1000 °C for 5 hours and washing with water, was investigated by degradation experiments of bisphenol A (BPA). A 500 mg L^{-1} BPA stock solution was prepared by dissolving 25 mg of BPA in 2 mL acetonitrile and slowly adding deionized water while stirring up to a final volume of 50 mL. The stock solution was used to prepare, in 250 mL blue cap bottles, new solutions, 200 mL at concentration 10 mg L^{-1} BPA, each one placed on a magnetic stirrer containing a heater (Fig. S2†). The temperature of the solution was set to 50 °C. The perovskites were added in concentration of 1 g L^{-1} at time = 0 min, and samples were collected at different times to follow the degradation of BPA.

The collected samples for each perovskite were filtered using a RC 0.45 μm syringe filter. The liquid phases were analyzed through HPLC using UV detection (Summit – Dionex). The column was a Kinetex 5 μm EVO C18 100 Å column (150 × 4.6 mm), the mobile phase flow was set to 1 mL min^{-1} (acetonitrile/water = 40/60), and UV detector set to measure at 230 nm. The concentration of BPA in each sample at different durations was calculated based on a calibration curve of BPA solutions with concentration up to 10 mg L^{-1}.

3. Results

3.1. Effect of cerium excess on the structural properties of Ce-doped $SrFeO_3$ perovskite-type materials

Fig. 1a displays the XRD patterns of all the synthesized Ce-doped $SrFeO_3$-based powders at increasing cerium content, from *Ce0*, where all cerium is dissolved in the perovskite matrix, to *Ce15*, with the maximum cerium excess in the powder (see also Table 1 for details on the nominal composition). In the XRD pattern of *Ce0*, only the characteristic peaks of the cubic Ce-doped $SrFeO_3$ were present and no other phases appeared. In the inset of Fig. 1a the XRD patterns of all the investigated Ce-doped strontium ferrate-based powders in the 46°–48° angular range are shown, evidencing the appearance of the XRD peak of CeO_2 (fluorite phase, F, at 47.7° 2θ) along with the main perovskite (P, 46.7° 2θ) phase, when cerium content overcomes the maximum solubility value (samples *Ce5*, *Ce10* and *Ce15*).

From the examination of the inset of Fig. 1a, it is also evident that cerium excess causes an enlargement of the peaks and

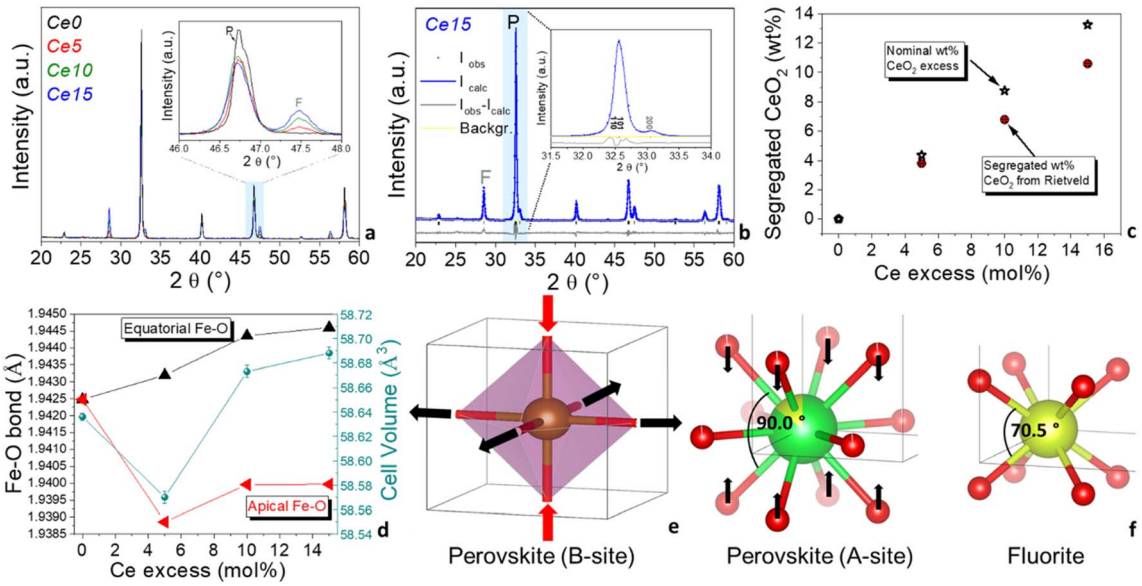

Fig. 1 (a) XRD patterns of all the investigated Ce-doped strontium ferrate powders, with the perovskite-type phase (P) and the CeO_2 fluorite-type phase (F) evidenced in the inset; (b) graphical Rietveld fitting and reflections of *Ce15* with tetragonal distortion; (c) wt% of segregated CeO_2 determined from Rietveld refinement and obtained from the nominal cerium excess; (d) trend of the Fe–O apical distances (red), equatorial distances (black) and cell volume (light blue) at increasing cerium excess; (e) graphical representation (VESTA software) of the apical and equatorial distortion at B-site of the perovskite; (f) graphical representation (VESTA software) of the Ce site of the P and of the F structures, evidencing the different oxygen geometry around cerium in the two structures.

a change in the peaks shape of the main perovskite. Effectively, Rietveld refinement results (Table S1†) suggest that the structure of the Ce-doped $SrFeO_3$ perovskite is tetragonally distorted (*P4/mmm*) when segregated CeO_2 is formed (samples *Ce5*, *Ce10* and *Ce15*), whereas it is perfectly cubic if there is no cerium excess (sample *Ce0*). In Fig. 1b, a Rietveld graphical fitting of a representative sample with the *P4/mmm* tetragonal structure is shown in a selected range of the XRD pattern. Quantitative analysis of the XRD patterns allowed to calculate the phase composition of the powders and the structural and microstructural parameters for each phase. In Fig. 1c, the trend of the experimental *vs.* nominal CeO_2 excess is reported. As expected, segregated CeO_2 increased linearly with nominal CeO_2 excess. The stars indicate the wt% CeO_2 calculated from the nominal mol% Ce excess. A slight underestimation was observed for the wt% CeO_2 obtained from Rietveld analysis, and the discrepancy with the nominal wt% CeO_2 increased with cerium excess (Fig. 1c). It is presumed that a poorly crystallized nanostructured CeO_2 was formed at the interface between perovskite and fluorite structures during the combustion process. The XRD pattern of a mechanical mixture (*MM*) prepared from CeO_2 and *Ce0*, using the same cerium excess as in *Ce15*, confirms that the structure of *MM* remained cubic, just like in the sample with no cerium excess (Fig. S3 and Table S1†). In addition, only fully crystallized CeO_2 was present, since nominal wt% of CeO_2 was almost identical to the wt% obtained from Rietveld analysis (Tables 1 and S1†). Looking at Table S1† and Fig. 1d it is worth noticing that cell volume of the perovskite slightly decreased and then increased with cerium excess. In parallel, the equatorial Fe–O bonds increased, and the apical Fe–O bonds decreased and then increase slightly, although they never reached the value calculated for *Ce0* (Fig. 1d). This can be ascribed to the tetragonal distortion of the B-site, where the octahedra flattened and expanded, as graphically shown in Fig. 1e. Since ceria is formed at lower temperatures than perovskite oxide, it is possible that during the self-combustion, the perovskite structure was forced to grow over the already formed CeO_2 fluorite lattice, which is also cubic, although cerium has a tetrahedral oxygen coordination and different angles (see Fig. 1f).

The smaller angles around cerium site in the fluorite structure may have induced the oxygens around cerium at the A-site of the perovskite to contract around cerium, decreasing the O–Ce–O angles. The effect on the cerium A-sites of the perovskite would be extended to the iron B-site through the oxygen bridges, also causing a distortion of the B-site, as observed from Rietveld refinement (Fig. 1d and e). This distortion causes a distancing of the equatorial oxygen moving toward a more reduced state of iron. Cerium oxide structure was also affected by this *in situ* growing. In fact, microstrain of this phase increased from about 500 to more than 2000 from *Ce5* to *Ce15* (Table S1†). Dai *et al.* also found a structural effect on the $LaFeO_3$ perovskite oxide, a shift of the perovskite peak caused by the decoration of increasing cerium oxide amount in $LaFeO_3$–CeO_2 electrocatalysts, although in that work the structure of $LaFeO_3$ remained orthorhombic regardless of the percentage of CeO_2 decoration.[36]

X-ray photoelectron spectroscopy (XPS) was performed to evaluate differences at surface level induced by the presence of segregated ceria. Fig. 2 shows the O 1s, Fe 2p, and Sr 3d region of the samples and in Table S2† the binding energy and the relative abundance of the different components are reported.

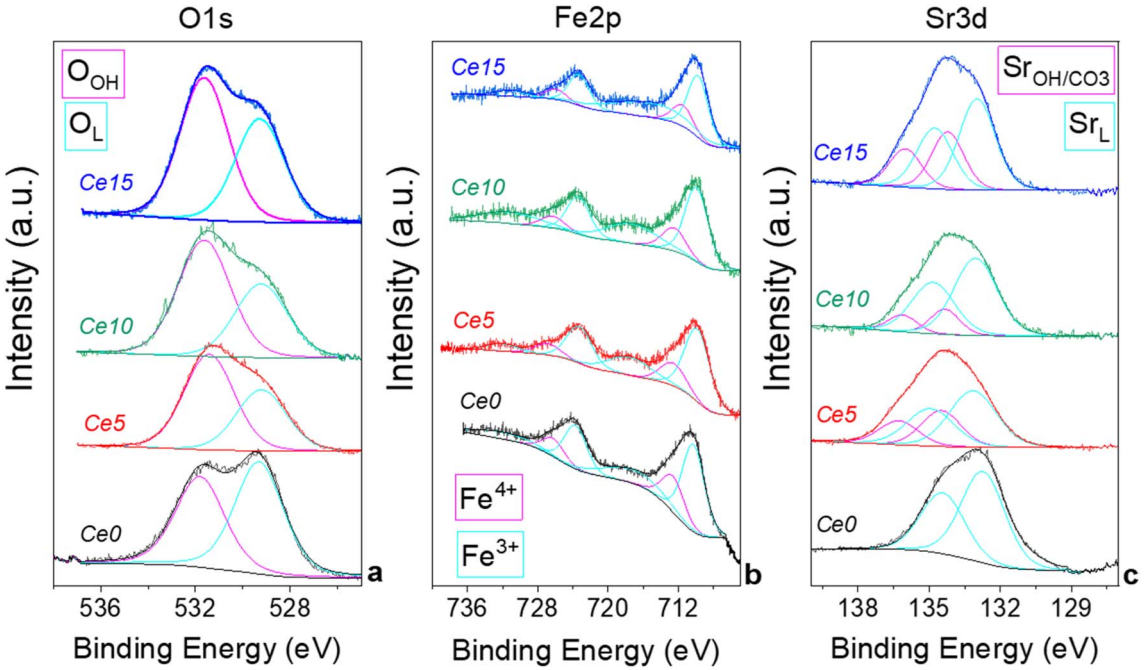

Fig. 2 X-ray photoelectron spectroscopy spectra of the investigated samples: (a) O 1s region, where O_L and O_{OH} represent the lattice oxygen and the surface oxygen, respectively; (b) Fe 2p region where Fe^{4+} and Fe^{3+} contributions are evidenced; (c) Sr 3d region., whereas Sr_L and $Sr_{OH/CO3}$ represent the Sr in the perovskite structure and the Sr in the $SrCO_3$ structure, respectively.

XPS measurements evidenced that the O 1s region is characterized by two components (Fig. 2a): O_L, at 529.6 eV, is attributed to oxygen in the perovskites lattice and O_H, at 531.5 eV, is attributed to adsorbed oxygen species and/or carbonates.[44] Differences in the ratio between the two oxygen components may be indicative of differences in the oxygen vacancies present in the materials. The highest O_L/O_H ratio is observed for *Ce0* indicating a lower number of oxygen vacancies present in the structure. It appears that the presence of cerium excess generates an increase of surface vacancies. Fe 2p region indicates that the presence of cerium excess influences slightly the state of iron, although all samples show the typical complex profile of Fe 2p region with the Fe $2p_{3/2}$/Fe $2p_{1/2}$ separation of 13.3 eV and the presence of a small shake up features. The main peaks can be deconvoluted into two components at *ca.* 710 and 712 eV which are attributed to Fe(III) and Fe(IV) respectively, in agreement with previous literature on Fe containing-compounds.[45,46] The relative percentage of the two iron species changes slightly along the series (Table S2†). In Fig. S4† the trend of Fe^{4+} with cerium excess is shown, evidencing that at the surface Fe^{4+} increases for low cerium excess and decreases again for larger cerium excess.

The initial increase of Fe^{4+} at the surface is probably caused by the tetragonal distortion induced by the *in situ* growth of the perovskite with excess ceria. A similar effect was observed in the bulk in Fig. 1d for the cell volume, that initially decreased, in agreement with the smaller ionic radius of Fe^{4+}, and then increased again for larger cerium excess. The Sr 3d region shows a peak, which is a convolution of Sr $3d_{5/2}$ and Sr $3d_{3/2}$ ($\Delta E = 1.8$ eV) (Fig. 2c). The shape of the peak points at the presence two doublets with the Sr $3d_{5/2}$ centered at *ca.* 133 eV and 134 eV, which, according to the more common interpretation, are attributed to Sr in the perovskite structure (Sr_L) and Sr in the $SrCO_3$ structure (Sr_{OH/CO_3}), respectively.[47,48] $SrCO_3$ is often formed in $SrFeO_3$-based compounds due to the high affinity of Sr for atmospheric CO_2 especially in the presence of humidity.[17] The presence of $SrCO_3$ on the surface could also be partially caused by the washing procedure (see experimental part). The presence of cerium excess seems to cause an increase of $SrCO_3$ on the surface (Table S2†), although it is not possible to identify a trend on the $SrCO_3$ surface content, probably due to the low surface area of these materials, which levels the differences at the surface. A thermal regeneration at 1000 °C in air on *Ce15* has the effect to decrease the surface $SrCO_3$ from 38 at% to 21 at%, whereas no oxygen or iron are modified by the treatment, which only causes the degradation of $SrCO_3$ and a re-incorporation of Sr in the perovskites structure. A comparison of XPS results of *Ce15* with those of the mechanical mixture *MM* (shown in Fig. S5 and Table S2†) confirms that the excess of ceria that was not grown *in situ* has a limited influence on the surface status of the elements and on the formation of oxygen vacancies.

3.2. Effect of cerium excess on microstructural, morphological, and textural properties of Ce-doped $SrFeO_3$ perovskite-type materials

Crystallite size and microstrain were calculated from Rietveld analysis of the diffraction data and reported in Table S1.† Crystallite size of perovskite phase was maintained between 230 and 430 nm, and that of fluorite ceria phase was maintained between 70 and 80 nm, irrespectively of the cerium excess

content. On the other hand, microstrain of both phases increased with cerium excess (Fig. 3a and Table S1†), suggesting that the microstructure of both the perovskite and the ceria phases was affected by the *in situ* growing during the combustion process. It is worth to note that microstrain of perovskite and fluorite phases in the mechanical mixture (*MM*) remained very close to the values registered for *Ce0* and CeO_2 samples (Fig. 3a and Table S1†). Porosity was below 0.02 $cm^3\ g^{-1}$ and surface area was generally under 10 $m^2\ g^{-1}$, as expected for perovskite-type materials and especially for $SrFeO_3$-based compounds[49] and both increased with cerium excess (Fig. 3b). It is supposed that the increase in surface area is mainly due to the increasing contribution of segregated ceria and especially of the poorly crystallized nanostructured one (see discussion of Fig. 1c). As a confirmation, surface area of the *MM* sample, which does not contain poorly crystallized ceria phase, did not reach the value registered for *Ce15* (Fig. 3b). SEM images in Fig. 4 compare *Ce0* and *Ce15* with CeO_2 and the mechanical mixture *MM*. From SEM images, it is evident that ceria and perovskite phases are intimately connected in *Ce15*, whereas the mechanical mixture *MM* shows separate islands of the two phases, although the phase composition in *Ce15* and *MM* is identical (Table S1† and Fig. 3c). Therefore, SEM results indicate that an inter-lattice heterostructure could have formed in *Ce15* between the perovskite and the fluorite lattices, as suggested in the previous sections and in agreement with the evident increase in microstrain with the increasing cerium excess observed in Fig. 3a.The existence of an inter-lattice heterostructure of *Ce15* compared to the *Ce0* + CeO_2 mechanical mixture is supported by the homogeneous distribution of Fe, Sr, and Ce in *Ce0* and *Ce15* detected through energy dispersive X-ray spectroscopy (Fig. S6†). On the other hand, the mechanical mixture shows a heterogeneous distribution visualized through the higher atomic density of Ce in areas with low content of Sr and Fe.

3.3. Effect of cerium excess on the redox properties of Ce-doped $SrFeO_3$ perovskite-type materials

The surface oxygen vacancy content of the materials was evaluated from TGA experiments by registering the desorption curves of adsorbed oxygen. The acquired TGA profiles related to the step 6 (see Experimental part, Section 2.2) are displayed in Fig. 5a. All the samples, after saturation with pure O_2, undergo to distinct weight losses under N_2. Total weight losses range from ~1 to 2.5 wt% (Fig. 5a). The weight loss between 300–600 °C was considered to evaluate the oxygen removed from the surface oxygen vacancies of the sample, whereas above 600 °C the removal of bulk oxygen usually occurs. It results that all the samples with cerium excess contain more oxygen vacancies than *Ce0* below 600 °C (Fig. 5), whereas the mechanical mixture shows an oxygen vacancy content comparable to that of *Ce0*. The slightly lower weight loss in *MM* is due to the smaller amount of perovskite in the mechanical mixture compared to *Ce0*, given that *MM* contains also CeO_2.

These findings suggest that the tetragonal distortion of the perovskite (Fig. 1) and the incremented microstrain (Fig. 3) increase the amount of oxygen that can be chemisorbed and thus released under N_2 flow at relatively high temperature. Most of the exposed results, along with the evidence of a tetragonal distortion with cerium excess, agree with the findings of Enriquez *et al.*,[21] where the oxygen content of a $SrFeO_3$ thin film was correlated with its structural and functional properties. Looking at the temperature range between 600–1000 °C, the weight loss, ranging between ~0.5–1.5%, increases in the order *Ce15* > *Ce10–Ce5* > *Ce0*, pointing out to the highest oxygen mobility of the *Ce15*, in line with the increment of lattice oxygen observed by XPS characterization on the surface of the powders (Fig. 2).

The reducibility of the $Sr_{0.86}Ce_{0.14}FeO_3$–CeO_2 powders with different cerium excess was investigated by temperature programmed reduction technique (TPR) by flowing 5 vol% H_2/Ar in the range between room temperature and 1000 °C. The TPR profiles of the samples *Ce0*, *Ce5*, *Ce10*, and *Ce15* are displayed in Fig. 5b, to visualize the effect of increasing cerium excess, whereas the reduction temperatures (divided in low, medium, and high temperature zones) and H_2 consumptions for all samples are listed in Table 2. The TPR profile of the *Ce0* perovskite is characterized by two main peaks, the first one centered at 450 °C and the second one above ~750 °C with maximum at around 1000 °C. According with our previous investigation of Ce-doped strontium ferrates,[22] the low

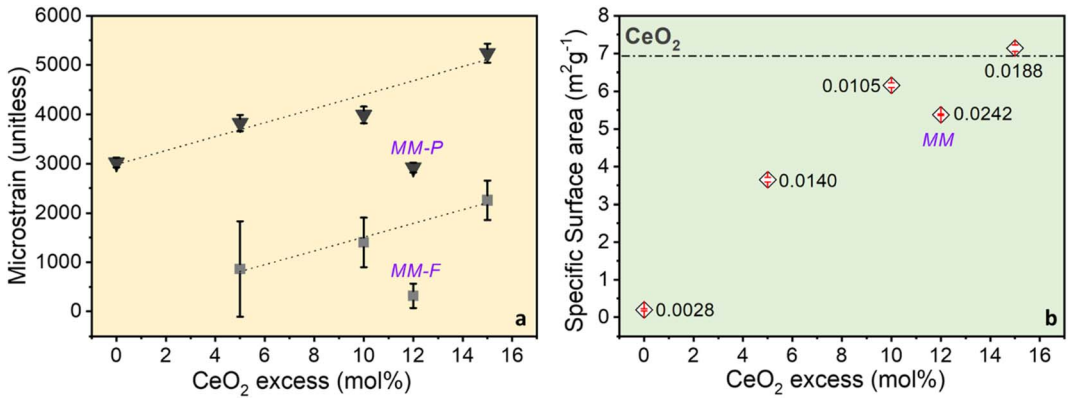

Fig. 3 (a) Microstrain trend of Ce-doped $SrFeO_3$ perovskite (P) and CeO_2 fluorite (F) structures with increasing cerium excess; (b) trend of surface area with increasing cerium excess; the numbers close to each symbol indicate relative cumulative pore volume on desorption ($cm^3\ g^{-1}$).

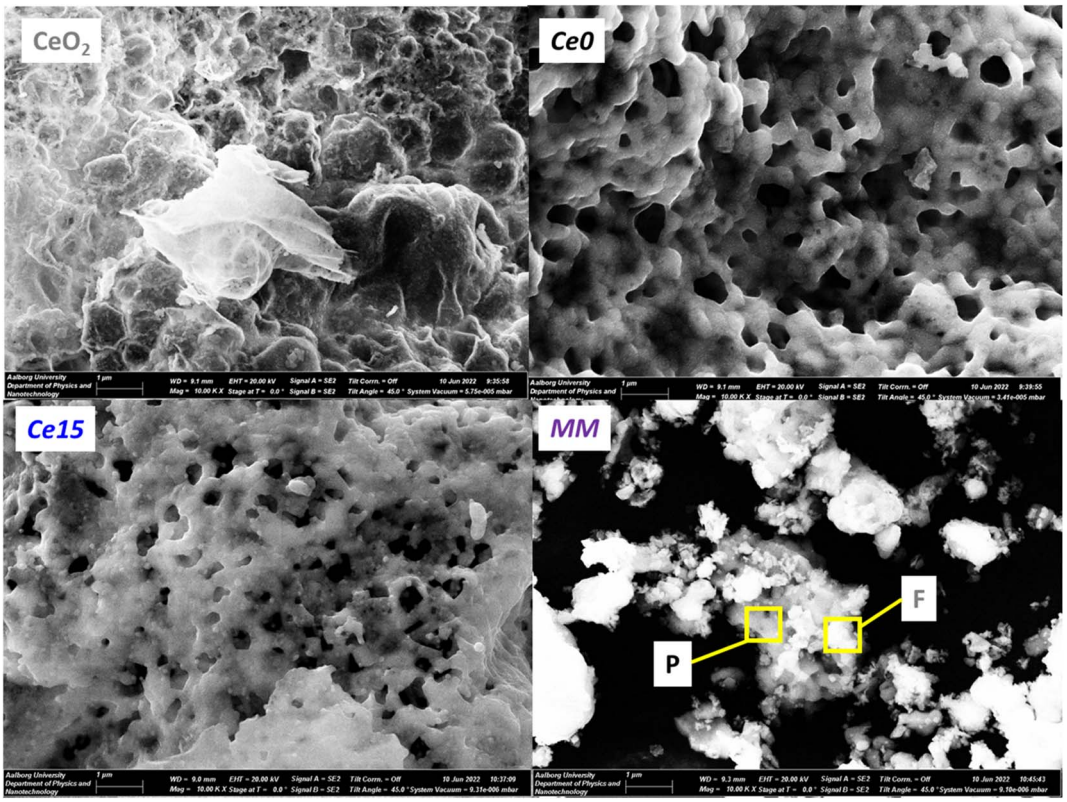

Fig. 4 SEM images of CeO_2, *Ce0*, *Ce15* and *MM*. In *MM*, the darker perovskite (P) and lighter fluorite (F) grains are highlighted in agreement with the EDX results in Fig. S6.†

temperature peak is ascribed to the reduction of Fe^{4+} species, present in the perovskite, to Fe^{3+}. Based on the chemical composition, the mmol g^{-1} of Fe, and considering the hydrogen consumption of the first peak (Table 2), the percentage of Fe^{4+} reduced to Fe^{3+} was calculated and corresponds to 44.5%. Assuming that in the region 550–700 °C only reduction of Ce^{4+} occurs as suggested in literature,[50] the percentage of Ce^{4+} reduced to Ce^{3+} was found to be 88%. Finally, supposing that no Fe^{2+} is present in the starting perovskite, *Ce0*, and attributing the reduction peak above ~750 °C only to the reduction of Fe^{3+} to Fe^{2+}, the extent of reduction Fe^{3+} to Fe^{2+} was estimated as 83.9%. By comparing the TPR curves of *Ce0* with those of *Ce5*, *Ce10* and *Ce15*, the effect of cerium excess addition is a progressive shift of the first reduction peak at lower temperature from 450 to 350 °C (Fig. S7a†). Such findings agree with recent literature.[23] Looking at the values listed in Table 2, the

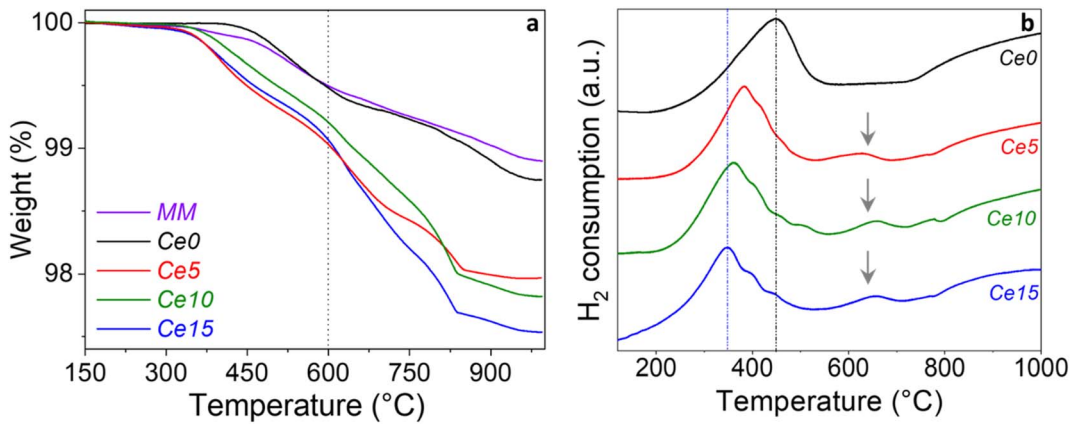

Fig. 5 (a) TGA graph of the investigated $SrFeO_3$-based powders prepared with different cerium excess and comparison with the mechanical mixture; (b) comparison between TPR of *Ce0*, *Ce5*, *Ce10* and *Ce15*. The TPR peak at around 650 °C is evidenced by an arrow only in the powders with some cerium excess.

Table 2 Reduction temperature and H_2 consumption obtained by TPR analysis of the investigated samples. The accuracy of hydrogen consumption evaluated through TPR measurements is ±5% and the temperature of peaks is quoted with an uncertainty of ±15 °C

Sample	*Ce0*	*Ce5*	*Ce10*	*Ce15*	CeO_2	*MM*
Ce content (mmol g^{-1})	0.70	0.91	1.11	1.29	5.81	1.25 (0.630 *Ce0*), (0.616 CeO_2)
Fe content (mmol g^{-1})	5.03	4.83	4.63	4.45	—	4.5
T_{peak} (°C) (low *T*)	450	385	362	350	375	415
H_2 uptake (mmol g^{-1})	1.12	1.01	0.95	1.53	0.46	1.05
T_{peak} (°C) (medium *T*)	Range 550–700	630; 775	658; 780	655; 780	—	Range 550–700
H_2 uptake (mmol g^{-1})	0.31	0.41	0.49	0.84	—	0.28
T_{peak} (°C) (high *T*)	1000	1000	1000	1000	870	1000
H_2 uptake (mmol g^{-1})	2.11	1.48	1.26	2.09	1.66	2.10

hydrogen uptake of this low temperature peak decreased from 1.12 mmol g^{-1} (*Ce0*) to 1.01 (*Ce5*) and to 0.95 mmol g^{-1} (*Ce10*). In parallel, the percentage of Fe^{4+} reduced to Fe^{3+} decreased from 44.5% (*Ce0*) down to 41.0% (*Ce10*).

It should be reminded that Ce and Fe content (mmol g^{-1}) were calculated considering that each sample has the nominal chemical composition indicated in Table 1 (second column) and TPR calculations were made by considering the change in Fe content. Therefore, the nominal composition $Sr_{0.86}Ce_{0.14}FeO_3$ that is 100% for the sample *Ce0*, decreases depending on the Ce excess as listed in Table 1. The so far reported shift of the first peak to lower temperatures (Table 2 and Fig. S7a†) and the lowered hydrogen uptake of the low temperature peak (Table 2) suggest that the introduction of Ce excess reduces the stability of Fe^{4+} ions in the perovskite structure, making them easier to be reduced. XRD and XPS results had indicated a similar trend (see Section 3.1), although both the characterization techniques evidenced that, initially, (from *Ce0* to *Ce5*) an opposite trend occurred, *i.e.*: an increase in Fe^{4+} percentage. This apparent discrepancy is explained by the different type of techniques that are compared. XRD and XPS observe the sample in its state, whereas TPR observes the powder *in situ* after a perturbation with an H_2 flow and temperature. What is surely concluded from the comparison between the three techniques is that Fe^{4+} formed upon the progressive tetragonal distortion becomes less stable and more reactive and tends to convert to Fe^{3+}.

Surprisingly, H_2 consumption of the first peak increased again for the *Ce15* sample, although, in agreement with the trend from *Ce0* to *Ce15*, exhibited the lowest reduction temperature. Such effect was explained assuming that reduction of Fe^{4+} ions, present in the perovskite phase, occurred along with surface reduction of the segregated ceria which takes place at 350 °C (Table 2), and that, by increasing the Ce mol% excess, the presence of CeO_2 crystalline phase increased accordingly, as clearly detected by XRD results.

Looking at the range around 550–700 °C, two distinct peaks were observed for *Ce5*, *Ce10*, and *Ce15* with H_2 uptake increasing from 0.31 mmol g^{-1} (*Ce0*) up to 0.84 mmol g^{-1} (*Ce15*). In agreement with the so far discussed crystallization of an isolated ceria phase, the increased H_2 amount was ascribed to the reduction of defective CeO_2 whose reduction overlaps with that of Ce^{4+} ions into the perovskite lattice (see *Ce0*). According with the literature[51,52] the crystallite size, the presence of grain boundaries, and defects in ceria crystallites may affect the peak shape and reduction temperature, thus explaining the observed difference with respect to the reduction profile typical of pure CeO_2 (see Fig. 5b).

As far as it concerns the high temperature reduction peaks (above ~750 °C) observed for *Ce0*, *Ce5*, *Ce10*, and *Ce15*, it is worth noting that the H_2 consumption decreased from 2.11 mmol g^{-1} (*Ce0*) to 1.26 mmol g^{-1} (*Ce10*) and, consequently the estimated percentage of Fe^{3+} reduced to Fe^{2+} decreased from 83.9% (*Ce0*) to 54.4% (*Ce10*). Conversely, an increased H_2 uptake occurred for the high temperature peak of *Ce15* that can be explained assuming that for such sample, containing the highest Ce mol% excess, well crystallized CeO_2 phase is formed that gives rise to reduction peaks typical of surface reduction at 350 °C as well as to bulk reduction, likely in the region ~550–700 °C and above ~750 °C. However, the exact range of temperature depends on the ceria crystallite site, defective structure, surface area and other factors, thus making impossible a separate estimation of the extent of Fe^{3+} and of Ce^{4+} reduction in the high temperature region.

The TPR profiles of pure CeO_2, the mechanical mixture (MM) along with *Ce0* and *Ce15* are compared in Fig. S7b and discussed in a dedicated section under the same figure.†

3.4. Effect of cerium excess on the thermocatalytic degradation of bisphenol a by Ce-doped $SrFeO_3$ perovskite-type materials

The concentration of bisphenol A (BPA) decreases continuously with time for all samples with *Ce15* degrading the most in 180 min (~68% of the BPA) and the *MM* degrading the least (48%) (Fig. 6a). Based on this, the reaction kinetic is described by the kinetic constant for a pseudo-first order reaction asusually found for this type of materials,[16] as seen from the linearized $\ln(c/c_0)$ *vs.* time plots (Fig. S8†). The nominal cerium excess greatly influences the kinetic rate for the *in situ* grown biphase ceria–perovskite catalysts showing a significant increase in the catalytic activity (Fig. 6b). In contrast, the kinetic rate decreases from *Ce0* to *MM* indicating structural changes in the *in situ* grown compounds must be beneficial. The decrease of thermocatalytic activity with *MM* might be a result of the smaller concentration *Ce0* in *MM* as it is partly substituted by CeO_2. The excess ceria greatly enhances the catalytic performance in the abatement of BPA. However, no degradation of BPA is observed when pure ceria synthesized by solution

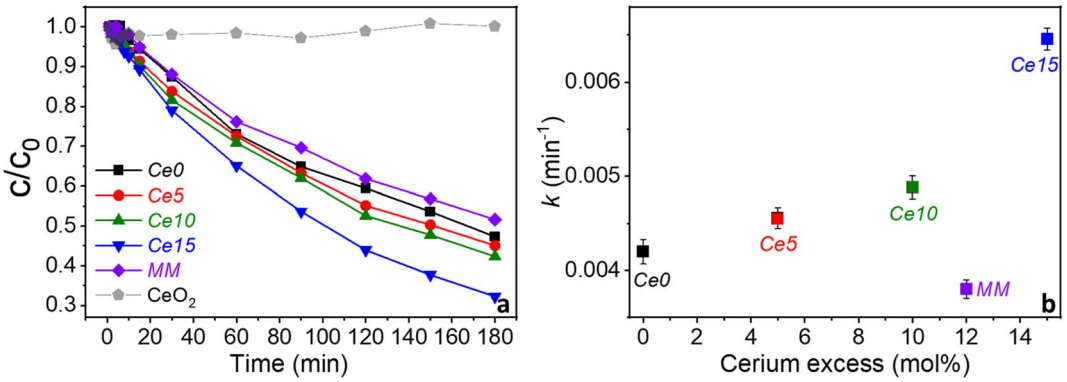

Fig. 6 (a) Thermocatalytic abatement of bisphenol A (initial concentration 10 mg L^{-1}) at 50 °C for perovskites (1 g L^{-1}) with excess ceria and the mechanical mixture (*MM*) and (b) change in kinetic constant (*k*) with increasing excess ceria and comparison with the mechanical mixture. Errors in (a) are smaller than the size of the symbols, whereas in (b) the errors are indicated in the graph for each *k* value.

combustion synthesis rather than perovskite was used as a catalyst (Fig. 6a, grey curve). This suggests that ceria, and possibly other metal oxides, can indirectly enhance the catalytic performance of perovskites, when they are *in situ* grown during the synthesis process, by altering the perovskite structure. To be beneficial, the excess of metal oxide needs to be formed in association with the growth of the perovskite nanocrystals during the synthesis, as confirmed by the fact that the mechanical mixture kinetic was like that of pure $Sr_{0.86}Ce_{0.14}FeO_{3-\delta}$ rather than like that of *Ce15* with 15 mol% excess cerium. In this conditions, structural changes (distortion) occur in the crystal structure of Ce-doped $SrFeO_3$ causing the largest effect on the catalytic activity.

Hammouda *et al.* found that a physical mixture of $LaCuO_3$ and CeO_2 resulted in complete catalytic degradation of bisphenol F through activation of hydrogen peroxide suggesting that ceria could cleave hydrogen peroxide.[25] Thus, this makes it different to this study where no additional chemicals were added, and the improved catalytic activity is caused by beneficial structural changes. Also, Hammouda *et al.* did not deeply investigate any structural changes upon physical mixing.[25] It can be postulated that oxygen vacancies play a direct role in the thermocatalytic performance of $Sr_{0.86}Ce_{0.14}FeO_{3-\delta}$ and that the tetragonal distortion caused by the co-growth of perovskite and ceria phases favors an increase of the oxygen vacancies content, as hypothesized elsewhere,[18] and oxygen mobility in the perovskite, enhancing its thermocatalytic activity. In facts, for PO–ceria biphasic systems with different perovskite composition and for reactions at much higher temperatures, Bork *et al.* suggested that a possible cause of ceria–perovskite synergy in solar thermochemical production could be the enhanced oxygen adsorption and diffusion processes at the ceria nano interface.[29] Other authors hypothesized that the perovskite could get further oxygen supply from ceria in BaSrCo-based perovskite–ceria composites, thus increasing the gas production through chemical-looping steam methane reforming.[28] In this work, the effect of ceria on the PO–ceria biphasic system was indirect, since *in situ* ceria formation did not show activity itself, but induced a distortion of the perovskite iron site through the growth of an inter-lattice, as suggested from structural, microstructural, morphological, textural, redox and chemical analysis on the investigated samples. Although ceria nanoparticles are only considered a minor environmental risk,[53] using cerium excess higher than 15 mol% would not be convenient, since it would probably decrease the inter-lattice zone between ceria and perovskite, favoring the formation of separate phases.

4. Conclusion

Excess cerium in Ce-doped $SrFeO_3$ perovskite oxides, segregates as crystalline fluorite-type CeO_2 phase during the formation of Ce-doped $SrFeO_3$ perovskite, has a profound influence on the perovskite structure itself, and favors the formation of an amorphous and highly defective interface between perovskite and fluorite phases. In particular, structural and redox properties of Ce-doped $SrFeO_3$ prepared in one-pot by solution combustion synthesis are greatly improved using cerium excess in the formulation, and the final properties of the perovskite oxide–oxide biphasic system are not the sum of the single constituents, as demonstrated by the comparison with a mechanical mixture. The positive effect is extended to the thermocatalytic performance and the powder with the highest cerium excess examined (15 mol% Ce excess) displays the highest thermocatalytic activity. It has been clearly evidenced that the perovskite prepared in one-pot together with excess of ceria precursor is connected to the fluorite structure of ceria through oxo-bonds and forced to grow *in situ* with a tetragonal distortion. The distortion of the perovskite phase in the perovskite oxide-based powders increases the number of oxygen vacancies and their mobility with increasing of cerium excess and this is beneficial for the thermocatalytic reaction. Likewise, the destabilization of Fe^{4+} in the perovskite structure with increasing cerium excess promotes the thermocatalytic reaction, through an enhancement of the redox potential. These findings suggest a new perspective for the investigation and application of perovskite oxide/oxide biphasic powders with catalytic properties, grown *in situ* during a one-pot synthesis. In

view of their technological application in water cleaning, the boosted thermocatalytic activity of the $Sr_{0.86}Ce_{0.14}FeO_3$–CeO_2 biphase allows decreasing the operation temperature and increasing the energy efficiency of the thermocatalytic system for application in wastewater cleaning.

Author contributions

Martin B. Østergaard: formal analysis, investigation, conceptualization, writing – original draft. Francesca Deganello: investigation, conceptualization, project administration, visualization, writing – original draft, writing – review & editing. Valeria La Parola: investigation, writing – review & editing. Leonarda F. Liotta: investigation, writing – review & editing. Vittorio Boffa: conceptualization, writing – review & editing. Mads K. Jørgensen: funding acquisition, resources, writing – review & editing.

Conflicts of interest

There are no conflicts to declare.

Acknowledgements

We thank Villum Fonden for financial support under grant no. 00028236. This research was partially funded under Eurostars joint programme, grant number E!113844, NanoPerWater project. CNR-ISMN technicians Nunzio Gallì and Francesco Giordano are acknowledged for their help in N_2-adsorption and X-ray diffraction experiments, respectively.

References

1 C. Li, K. C. K. Soh and P. Wu, *J. Alloys Compd.*, 2004, **372**, 40–48.
2 R. J. D. Tilley, *Perovskites: Structure-Property Relationships*, 2016.
3 Z. Zeng, Y. Xu, Z. Zhang, Z. Gao, M. Luo, Z. Yin, C. Zhang, J. Xu, B. Huang, F. Luo, Y. Du and C. Yan, *Chem. Soc. Rev.*, 2020, **49**(4), 1109–1143.
4 K. Wang, C. Han, Z. Shao, J. Qiu, S. Wang and S. Liu, *Adv. Funct. Mater.*, 2021, **31**, 1–31.
5 J. Zhu, H. Li, L. Zhong, P. Xiao, X. Xu, X. Yang, Z. Zhao and J. Li, *ACS Catal.*, 2014, **4**, 2917–2940.
6 A. Varma, A. S. Mukasyan, A. S. Rogachev and K. V. Manukyan, *Chem. Rev.*, 2016, **116**, 14493–14586.
7 F. Deganello and A. K. Tyagi, *Prog. Cryst. Growth Charact. Mater.*, 2018, **64**, 23–61.
8 L. Zhang, Y. Zhang, J. Wei and W. Liu, *Chem. Eng. J.*, 2021, **403**, 126386.
9 E. Bilgin Simsek and Ö. Tuna, *J. Phys. Chem. Solids*, 2023, **176**, 111276.
10 M. Zhu, J. Miao, D. Guan, Y. Zhong, R. Ran, S. Wang, W. Zhou and Z. Shao, *ACS Sustainable Chem. Eng.*, 2020, **8**, 6033–6042.
11 J. Jing, C. Cao, S. Ma, Z. Li, G. Qu, B. Xie, W. Jin and Y. Zhao, *Chem. Eng. J.*, 2021, **407**, 126890.
12 H. Jeong, Y. H. Kim, B.-R. Won, H. Jeon, C. Park and J. Myung, *Chem. Mater.*, 2023, **35**, 3745–3764.
13 W. Zhang, Z. Liu, P. Chen, G. Zhou, Z. Liu and Y. Xu, *Int. J. Environ. Res. Public Health*, 2021, **18**, 4906.
14 M. B. Østergaard, A. B. Strunck, M. K. Jørgensen and V. Boffa, *J. Environ. Chem. Eng.*, 2021, **9**, 106749.
15 M. L. Tummino, E. Laurenti, F. Deganello, A. Bianco Prevot and G. Magnacca, *Appl. Catal., B*, 2017, **207**, 174–181.
16 K. Janowska, V. Boffa, M. K. Jørgensen, C. Quist-Jensen, F. Hubac, F. Deganello, F. E. B. Coelho and G. Magnacca, *npj Clean Water*, 2020, **3**, 1–7.
17 M. B. Østergaard, A. B. Strunck, V. Boffa and M. K. Jørgensen, *Catalysts*, 2022, **12**, 265.
18 D. Palma, F. Deganello, L. F. Liotta, V. La Parola, A. Bianco Prevot, M. Malandrino, E. Laurenti, V. Boffa and G. Magnacca, *Inorganics*, 2023, **11**, 85.
19 F. E. Bortot Coelho, F. Nurisso, V. Boffa, X. Ma, F. A. O. Rasse-Suriani, P. Roslev, G. Magnacca, V. Candelario, F. Deganello and V. La Parola, *J. Water Process Eng.*, 2022, **49**, 102941.
20 V. D. Sedykh, O. G. Rybchenko, E. V. Suvorov, A. I. Ivanov and V. I. Kulakov, *Phys. Solid State*, 2020, **62**, 1916–1923.
21 E. Enriquez, A. Chen, Z. Harrell, P. Dowden, N. Koskelo, J. Roback, M. Janoschek, C. Chen and Q. Jia, *Sci. Rep.*, 2017, **7**, 1–8.
22 F. Deganello, L. F. Liotta, A. Longo, M. P. Casaletto and M. Scopelliti, *J. Solid State Chem.*, 2006, **179**, 3406–3419.
23 X. Tian, C. Zheng and H. Zhao, *Appl. Catal., B*, 2022, **303**, 120894.
24 V. C. Belessi, T. V. Bakas, C. N. Costa, A. M. Efstathiou and P. J. Pomonis, *Appl. Catal., B*, 2000, **28**, 13–28.
25 S. Ben Hammouda, F. Zhao, Z. Safaei, I. Babu, D. L. Ramasamy and M. Sillanpää, *Appl. Catal., B*, 2017, **218**, 119–136.
26 K. Wang, H. Niu, J. Chen, J. Song, C. Mao, S. Zhang, S. Zheng, B. Liu and C. Chen, *Materials*, 2016, **9**, 1–12.
27 X. Gao, Z. Jin, R. Hu, J. Hu, Y. Bai, P. Wang, J. Zhang and C. Zhao, *J. Rare Earths*, 2021, **39**, 398–408.
28 H. Ding, C. Luo, X. Li, D. Cao, Q. Shen and L. Zhang, *Fuel*, 2019, **253**, 311–319.
29 A. H. Bork, A. J. Carrillo, Z. D. Hood, B. Yildiz and J. L. M. Rupp, *ACS Appl. Mater. Interfaces*, 2020, **12**, 32622–32632.
30 J. Kirchnerova, M. Alifanti and B. Delmon, *Appl. Catal., A*, 2002, **231**, 65–80.
31 Q. Yang, L. Chen, N. Jin, Y. Zhu, J. He, P. Zhao, C. Huang, L. Wei, X. Ma and X. Wang, *Appl. Catal., B*, 2023, **330**, 122636.
32 A. A. Ansari, S. Adil, M. Alam, M. Assal, J. Labis and A. Alwarthan, *Sci. Rep.*, 2020, **10**, 15012.
33 M. Alifanti, J. Kirchnerova and B. Delmon, *Appl. Catal., A*, 2003, **245**, 231–244.
34 C. Yang, X. Yu, S. Heißler, P. G. Weidler, A. Nefedov, Y. Wang, C. Wöll, T. Kropp, J. Paier and J. Sauer, *Angew. Chem., Int. Ed.*, 2017, **56**, 16399–16404.
35 D. C. Grinter, M. Allan, H. J. Yang, A. Salcedo, G. E. Murgida, B.-J. Shaw, C. L. Pang, H. Idriss, M. V. Ganduglia-Pirovano and G. Thornton, *Angew. Chem.*, 2021, **133**, 13954–13958.

36 Y. Dai, J. Yu, Z. Zhang, C. Cheng, P. Tan, Z. Shao and M. Ni, *ACS Appl. Mater. Interfaces*, 2021, **13**, 2799–2806.
37 G. Magnacca, G. Spezzati, F. Deganello and M. L. Testa, *RSC Adv.*, 2013, **3**, 26352.
38 F. Deganello, M. L. Tummino, C. Calabrese, M. L. Testa, P. Avetta, D. Fabbri, A. B. Prevot, E. Montoneri and G. Magnacca, *New J. Chem.*, 2015, **39**, 877–885.
39 B. H. Toby and R. B. Von Dreele, *J. Appl. Crystallogr.*, 2013, **46**, 544–549.
40 B. H. Toby, *Powder Diffr.*, 2006, **21**, 67–70.
41 K. Momma and F. Izumi, *J. Appl. Crystallogr.*, 2011, **44**, 1272–1276.
42 S. Brunauer, P. H. Emmett and E. Teller, *J. Am. Chem. Soc.*, 1938, **60**, 309–319.
43 E. P. Barrett, L. G. Joyner and P. P. Halenda, *J. Am. Chem. Soc.*, 1951, **73**, 373–380.
44 A. Yan, V. Maragou, A. Arico, M. Cheng and P. Tsiakaras, *Appl. Catal., B*, 2007, **76**, 320–327.
45 M. Wu, S. Chen and W. Xiang, *Chem. Eng. J.*, 2020, **387**, 124101.
46 H. Hu, Q. Zhang, C. Wang, M. Chen and Q. Wang, *Chem. Eng. J.*, 2022, **435**, 134894.
47 J. Kuyyalil, D. Newby, J. Laverock, Y. Yu, D. Cetin, S. N. Basu, K. Ludwig and K. E. Smith, *Surf. Sci.*, 2015, **642**, 33–38.
48 M. V. Bukhtiyarova, A. S. Ivanova, E. M. Slavinskaya, L. M. Plyasova, V. A. Rogov, V. V. Kaichev and A. S. Noskov, *Fuel*, 2011, **90**, 1245–1256.
49 F. Deganello, G. Marcí and G. Deganello, *J. Eur. Ceram. Soc.*, 2009, **29**, 439–450.
50 E. M. Iwanek (nee Wilczkowska), L. F. Liotta, S. Williams, L. Hu, H. Ju, G. Pantaleo, Z. Kaszkur, D. W. Kirk, W. Patkowski and M. Gliński, *Catalysts*, 2022, **12**, 524.
51 H. Zhu, Z. Qin, W. Shan, W. Shen and J. Wang, *J. Catal.*, 2004, **225**, 267–277.
52 L. F. Liotta, G. Di Carlo, F. Puleo, G. Marcì and G. Deganello, *Stud. Surf. Sci. Catal.*, 2010, **175**, 417–420.
53 C. J. Dedman, M. M. I. Rizk, J. A. Christie-Oleza and G. L. Davies, *Front. Mar. Sci.*, 2021, **8**, 571.